



Highly selective photocatalytic reduction of CO₂ to ethane over Au-O-Ce sites at micro-interface

Jixiang Ji^a, Ruru Li^a, Hao Zhang^a, Yingnan Duan^a, Qian Liu^a, Haozhi Wang^{b,*}, Zhurui Shen^{a,*}

^a School of Materials Science and Engineering and Smart Sensing Interdisciplinary Science Center, Nankai University, Tianjin 300350, China

^b State Key Laboratory of Marine Resource Utilization in South China Sea, School of Materials Science and Engineering, Hainan University, Haikou 300350, China

ARTICLE INFO

Keywords:

CO₂ photoreduction
Au-CeO₂ micro-interface
Au-O-Ce active sites
C₂ selectivity
Rare earth

ABSTRACT

To date, the efficient photocatalytic conversion of CO₂ into high-value C₂ products remains a great challenge. Herein, the Au-CeO₂ nanocomposite with Au-O-Ce sites at the micro-interface was developed to achieve a highly selective conversion of CO₂ into C₂H₆. This can be partially ascribed to the formation of key intermediates of COCO* was confirmed via in-situ Fourier transform infrared (FTIR) spectroscopy, indicating that the Au-CeO₂ micro-interface could prompt the multi-electron reduction of CO* before desorption, and enable the production of C₂ species. Moreover, theoretical calculations suggested that Au-O-Ce sites at the micro-interface could reduce the energy barriers for the formation of COOH* and COCO*, facilitating the production of C₂H₆. Therefore, the Au-CeO₂ nanocomposite exhibited a C₂H₆ production rate of 11.07 μmol g⁻¹ h⁻¹ and high electron selectivity of 93.1 % (product selectivity: 65.3 %), which is comparable with most state-of-the-art photocatalysts.

1. Introduction

Nowadays, the excessive emission of carbon dioxide has caused severe greenhouse effects, as a simple and potential way, photocatalytic conversion of CO₂ to valuable chemicals has attracted great attention [1–3]. However, the conversion of CO₂ to valuable chemicals is challenging because of the extremely high dissociation energy of the C=O bond in CO₂ (750 kJ mol⁻¹) [4]. Currently, the reported products of CO₂ photoreduction are mainly C₁ products such as methane [5], carbon monoxide [6], and methanol [7], depending on the high formation energy barrier for the intermediate COOH*. Recently, some reports have shown that CO₂ can be converted into C₂ products with higher energy density and economic value (such as ethylene [8], ethane [9], acetic acid [10], etc.) through slow multi-electron reduction and C-C coupling reaction [11]. However, both the multi-electron reduction and the coupling of C-C bonds should be driven by high energy generated by illumination; therefore, the C₂ product selectivity is low (in the range of 20–50 %) [8,12–14]. For example, Wang et al [12]. reported that Au/TiO_{2-x} composites could achieve 20.0 % selectivity for C₂H₆, and proposed a reaction mechanism based on the synergistic effect of Au localized surface plasmon resonance (LSPR) and oxygen vacancies (O_v) to improve C₂ selectivity. Zhao et al [13]. reported that the CuO_x@p-ZnO photocatalyst could promote C-C coupling and achieve a

selectivity of 32.9 % by anchoring CO on the catalyst surface and forming unique Cu⁺ sites on the CuO matrix; Dong et al [15]. synthesized a Cu_{0.8}Au_{0.2}/TiO₂ photocatalyst through a facile photodeposition method to achieve 11.9 % C₂H₄ product selectivity, and proposed the synergistic effect of Cu single atoms and Au-Cu alloys. Despite the significant progress, the evolution efficiency and selectivity to generate C₂ products are insufficient for future industrialization. Developing a novel photocatalyst with satisfactory efficiency and selectivity remains a significant challenge thus far. Moreover, these pioneer studies indicated that rational design of the photocatalyst interface, particularly constructing complex and synergistic metal active sites, was the key to the generation of C₂ products.

Rare earth nanomaterials, such as ceria [16], Pt-rare-earth element/zeolite [17], Tb-2,5-dihydroxyterephthalic acid [18], have been widely studied as heterogeneous catalysts for applications in the petrochemical industry as well as electrocatalysis and photocatalysis [19,20]. Ceria with two valence states (Ce³⁺ and Ce⁴⁺) can readily generate oxygen vacancies and act as an effective catalyst [21–23]. Recently, the excellent performance of CeO₂ as a photocatalyst for CO₂ conversion has been demonstrated. Wang et al [22]. reported that Cu/CeO_{2-x} composites could convert CO₂ with H₂O into CO with a yield of 8.25 μmol g⁻¹ h⁻¹ under xenon light irradiation, which was 26 times higher than that of pristine CeO_{2-x}. Sun et al [23]. have synthesized

* Corresponding authors.

E-mail addresses: hzwang001@tju.edu.cn (H. Wang), shenzhurui@nankai.edu.cn (Z. Shen).

<https://doi.org/10.1016/j.apcatb.2022.122020>

Received 8 August 2022; Received in revised form 11 September 2022; Accepted 24 September 2022

Available online 4 October 2022

0926-3373/© 2022 Elsevier B.V. All rights reserved.

Pd-CeO₂ nanosheets with Pd^{δ+}-Ce³⁺-O_V double sites, and its selectivity of CH₄ was ~100 %, compared with only 9 % when using pristine CeO₂ as a photocatalyst. Mechanistic investigations showed that Pd doping could lower the energy barriers of the crucial intermediates CHO* and CH₃O* for the generation of CH₄. These studies indicate that CeO₂ has significant potential for the efficient photocatalytic conversion of CO₂ into valuable chemicals. However, few reports have shown that C2 products can be effectively generated using CeO₂ as a unitary catalyst. This is mainly because the geometric configuration and electronic states of the active sites are not favorable to produce key intermediates of C2 products, such as COCO*. Therefore, the interface engineering of the CeO₂-based photocatalyst, particularly the development of appropriate active sites, is an essential way to prompt the generation of C2 intermediate.

Herein, Au-CeO₂ nanocomposite was developed with Au-O-Ce sites at the micro-interface to achieve a highly selective photocatalytic production of ethane from CO₂. Compared with pristine CeO₂, the theoretical calculations showed that the adsorption site of CO₂ changed from O_V sites on CeO₂ to Au-O-Ce sites on the nanocomposites. This crucial step determined the generation of key C2 intermediates, as confirmed via the in-situ Fourier transform infrared (FTIR) spectroscopy. In addition, the Au-CeO₂ micro-interface could ensure the multi-electron reduction of CO* before desorption, thereby facilitating the conversion of CO₂. Consequently, the nanocomposite showed a C₂H₆ evolution rate of 11.07 μmol g⁻¹ h⁻¹ and high electron selectivity of 93.1 % (product selectivity: 65.3 %). Its electron consumption rate reached a maximum of 171.4 μmol g⁻¹ h⁻¹, which was 42.85 times higher than that of pristine CeO₂. Besides, Au-CeO₂ nanocomposite could catalyze the reaction at low CO₂ concentrations, showing its substantial potential for large-scale applications in future.

2. Experimental details

2.1. Materials

All chemicals were used as received without further purification unless otherwise stated. Chloroauric acid (AR) was obtained from Xiya (China). Cerium oxide (99.5 %, 20–50 nm) and cupric oxide (99.5 %, 100–200 nm) were purchased from Macklin. Sodium borohydride (99 %, powder) was obtained from Acros Organics. Titanium oxide (99.8 % metal basis, 30 nm) was purchased from Aladdin.

2.2. Synthesis of Au solution

HAuCl₄ (1 g) was dissolved in deionized water (250.0 mL) with vigorous magnetic stirring for 0.5 h and ultrasonication for 0.5 h.

2.3. Synthesis of the Au/CeO₂ photocatalyst

The Au/CeO₂ photocatalyst was prepared using a water bath method described in the literature. Typically, 0.2 g of CeO₂ was dissolved in 40 mL of deionized water under stirring and ultrasound. Meanwhile, 3 mg of NaBH₄ and 0.88x mL Au solution were dissolved in 10 mL of deionized water with stirring to form a precursor solution. The Au precursor was then added dropwise to the CeO₂ solution under magnetic stirring in a water bath at 70 °C for 4 h. Finally, the obtained purple Au/CeO₂ solid was washed with deionized water and ethanol for several times and dried at 60 °C overnight. Based on the volume of 0.88x mL of the Au mixed solution, the Au/CeO₂ with different gold contents was labeled ACEO-x (x% = $\frac{m(\text{Au})}{m(\text{CeO}_2)}$), representing the mass proportion of Au in CeO₂.

2.4. Synthesis of Au/CuO and Au/g-C₃N₄ photocatalysts

The same synthesis method used for ACEO-x was employed for preparing Au/CuO and Au/g-C₃N₄, except that the matrix material CeO₂

was replaced with CuO and g-C₃N₄, respectively.

2.5. Synthesis of Cu/CeO₂ and Pt/CeO₂ photocatalysts

The same synthesis method as that of ACEO-x was used for synthesizing Cu/CeO₂ and Pt/CeO₂, except that the precursor Au solution was replaced with Cu and Pt solutions, respectively.

2.6. Characterizations

The morphologies of the samples were characterized via transmission electron microscopy (TEM) and high-resolution TEM (HRTEM) using a JEM-2800 microscope (JEOL, Japan), operating at an acceleration voltage of 200 kV. Aberration-corrected high-angle annular dark-field scanning transmission electron microscopy (HAADF-STEM) images were obtained at 300 kV using an FEI Titan Cubed Themis G2300 system. The crystalline structures were characterized via X-ray diffraction (XRD) using monochromatized Cu Kα radiation (Rigaku Smart Lab 3 kW). X-ray photoelectron spectroscopic (XPS) analysis was performed using a Thermal Scientific ESCALAB 250Xi instrument with an Al Kα radiation source. The photoelectrochemical performance was tested using a 760E electrochemical workstation with a three-electrode cell. Photoluminescence (PL) and time-resolved fluorescence spectra were recorded using a fluorescence spectrometer (FLS-1000) with an excitation wavelength of 350 nm and monitoring wavelength of 450 nm at room temperature. The photo-absorption performance of the materials was determined via ultraviolet–visible diffuse reflectance spectrum (UV-Vis DRS) with barium sulfate as a reference on a Shimadzu UV-3600 spectroscopy. The electron paramagnetic resonance (EPR) measurements were performed using a Bruker EMXPLUS system. The mass fraction of Au was measured using an Agilent 725ES inductively coupled plasma–optical emission spectroscopy (ICP-OES) system. In-situ Fourier transform infrared (FTIR) spectra were obtained using a Bruker TENSOR II Fourier Transform Infrared spectrometer. The gas products were quantified via gas chromatography–mass spectrometry (GC-MS; Agilent Technologies 7890B-5977 A).

3. Results and discussion

3.1. Microstructure and chemical properties

The Au-CeO₂ nanocomposite was composed of Au and CeO₂ nanocrystals with abundant micro-interfaces. This was studied using ACEO-3 as the example, via the TEM and HAADF-STEM analysis as follow (Fig. 1 (a)–(b), Fig. S1). As shown in the TEM and energy dispersive X-ray spectroscopy (EDS) images of ACEO-3 (Figs. S1 and S2), the Au nanocrystals were tightly combined with CeO₂ nanocrystals, and Ce and O were evenly distributed with the agglomerated Au. The HRTEM image (Fig. 1(a)) further showed that the Au and CeO₂ nanocrystals was approximately 5–10 nm. The CeO₂ nanocrystal tightly combined with an Au nanocrystal is shown in the center of the image with interplanar distances of 2.36 and 3.12 Å ascribed to the (111) crystal facets of Au and CeO₂ [23,24], respectively. Furthermore, HAADF-STEM analysis was performed to study the atomic structure of the micro-interface between the Au and CeO₂ nanocrystals. As shown in Fig. 1(b), the micro-interface could be observed at a scale of 1 nm. The Ce atoms (bright spots at the lower position) were in close contact with the Au crystal lattices, possibly leading to a certain degree of interfacial chemical bonding, for example, Au-O-Ce, which will be illustrated in detail via theoretical calculations in the mechanistic study [25]. In addition to ACEO-3, other ACEO-x samples with different quantities of Au nanocrystals were prepared for comparison (Fig. 1(c)–(f); Figs. S3–S8). The Au contents of ACEO-x (x = 0.5, 1, 3, 5) were 0.267, 0.654, 2.836, and 4.145 wt%, respectively (Table S1). As shown in Fig. 1 (c), all the ACEO-x samples showed similar XRD patterns ascribed to cubic phase CeO₂ (PDF#43–1002) [22]. Moreover, with an increase in

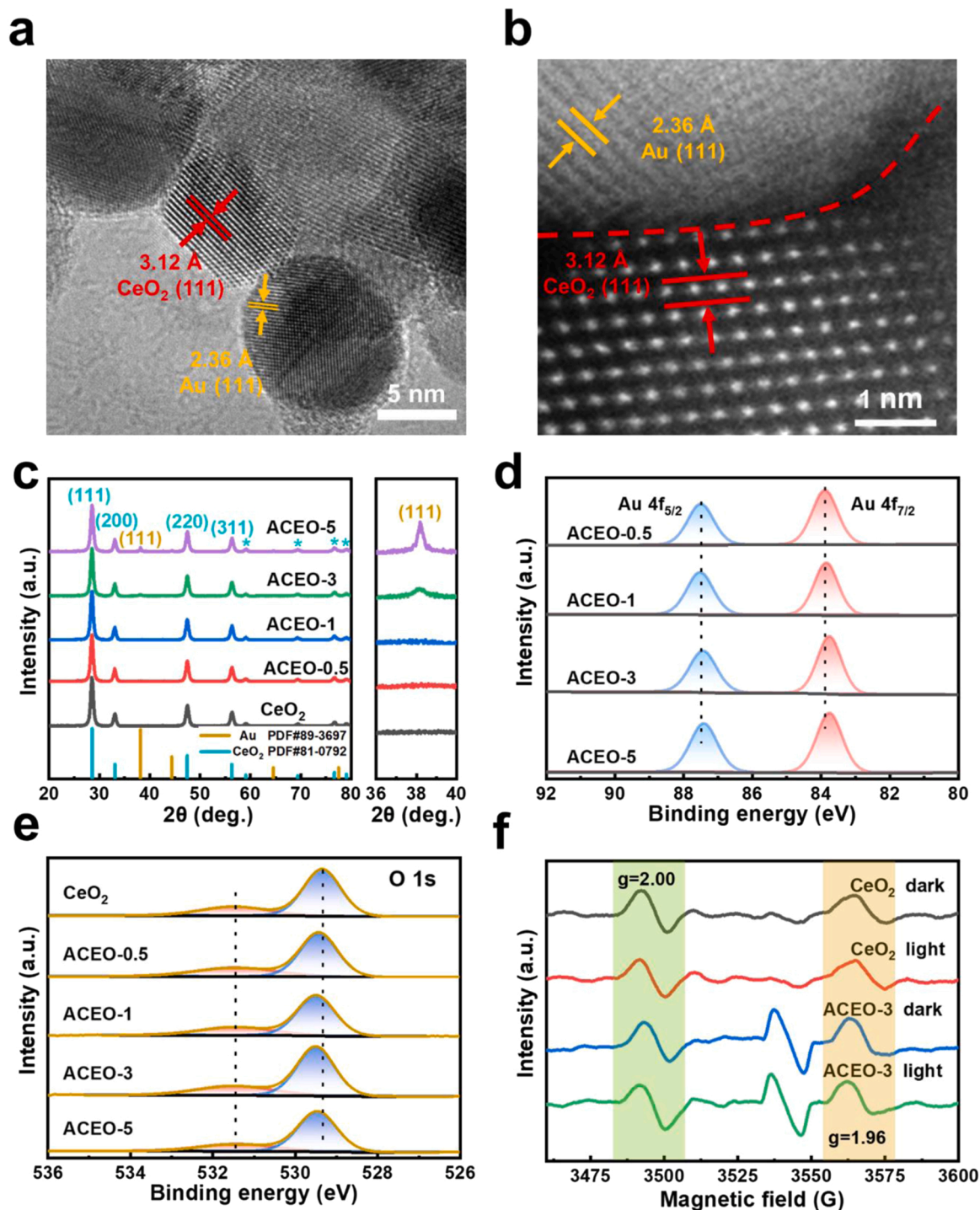


Fig. 1. (a) HRTEM and (b) HAADF-STEM images of ACEO-3. (c) XRD patterns, XPS spectra for (d) Au 4f and (e) O 1s, and (f) EPR spectra of ACEO-x samples.

the Au content, a new peak emerged at 38.1° , corresponding to the Au (111) crystal facet, further proving the successful combination of Au nanocrystals. In addition, with increasing Au content, the sample color became darker, and the size of the Au nanocrystals was slightly enlarged. (Figs. S3–S8).

To further study the surface chemical nature, XPS analysis was performed (Fig. 1(d)–(e) and Figs. S9 and S10). As shown in Fig. 1(d), with the increasing Au content, the binding energies (BEs) of Au 4f_{7/2} shifted negatively by 0.1 eV, and the BEs of Au 4f_{5/2} remained unchanged [15]. These results indicated that the Au nanocrystals were in the metallic state. However, the Au atoms at the micro-interface might gather more

electrons. Consistently, the peaks of O 1s are positively shifted by 0.18 eV with the increasing Au content (Fig. 1(e)), indicating a decrease in the electron density of O atoms at the micro-interface. These results suggested the existence of a Au-O-Ce atomic structure at the micro-interface of Au-CeO₂, where the O atoms donated electrons to the Au atoms and generated possible active sites for CO₂ photoreduction. The EPR spectra (Fig. 1(f)) show that both pristine CeO₂ and ACEO-3 exhibit two Ce³⁺ signals with g factors of 1.96 and 2.00, respectively [7,26]. The unsaturated coordination of Ce³⁺ ions facilitated the formation of O_V sites around it. Similarly, in the Raman spectra (Fig. S11), the peak at 460 nm further confirms the existence of O_V sites [22].

Notably, the intensity of the Ce^{3+} signal in ACEO-3 was consistent with that of CeO_2 under dark conditions, indicating that they had a similar concentration of oxygen vacancies, and the introduction of Au nanocrystals did not change the concentration of O_V sites. Under simulated light irradiation, the oxygen vacancies of all samples remained unchanged, indicating that the light irradiation did not affect the oxygen vacancies. The specific role of the O_V sites was further explained in the mechanistic study.

3.2. CO_2 photoreduction performance of catalysts

The photocatalytic CO_2 reduction performance was evaluated by irradiating the catalyst with simulated solar light in a gas-solid reaction system (Fig. 2(a)). The main products detected in this system were carbon monoxide and ethane. The CO_2 photoreduction activity of pristine CeO_2 manifested with a CO production rate of $2.02 \mu\text{mol g}^{-1} \text{h}^{-1}$, and C_2H_6 was not detected during the 4 h illumination period. In contrast, with an increase in the Au content, the main product shifted

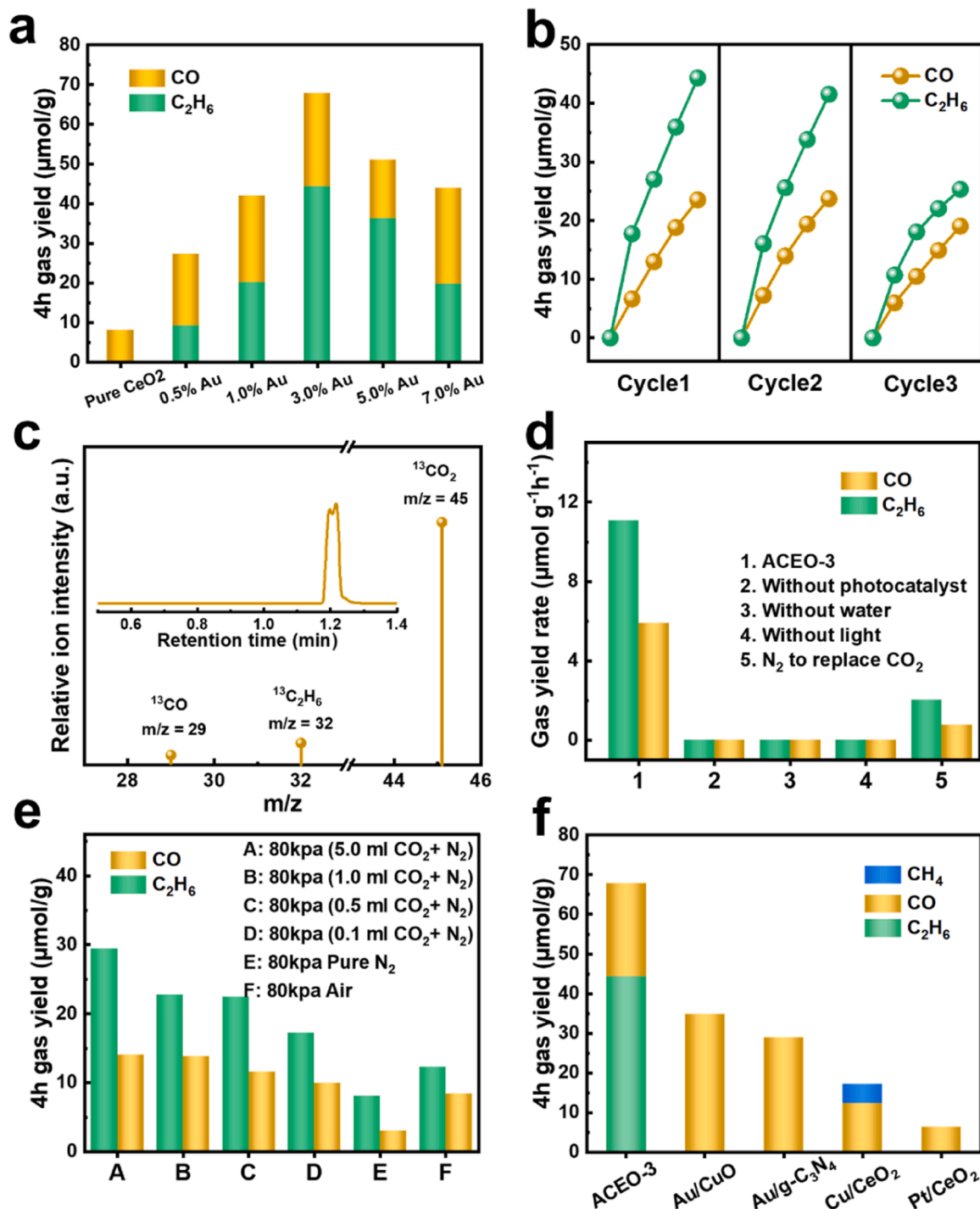


Fig. 2. CO_2 photoreduction properties of samples. (a) CO and C_2H_6 formation yield as a function of the Au content for ACEO-x. (b) Cycle activity test of the photocatalytic CO_2 reduction process over ACEO-3. (c) ^{13}C isotope analysis spectrum of the products on ACEO-3 after 4 h xenon-light irradiation under a humid CO_2 atmosphere. (d) Control group experiments to eliminate the effects of systematic errors or irrelevant variables. (e) Photocatalytic activity of ACEO-3 at different concentrations of CO_2 . (f) Gas yield of photocatalytic CO_2 reduction using ACEO-3, Au/CuO, Au/g- C_3N_4 , Cu/CeO₂, and Pt/CeO₂ as catalysts.

from CO to C₂H₆. The rate of the CO₂ reduction reaction (CO₂RR) firstly increased and then decreased. This was because when further increasing the Au content, more Au nanoparticles would cover larger surface of the CeO₂. This brought the smaller light-absorbing area of CeO₂ and the reduced CO₂ adsorption capacity of the catalyst. When the Au content was 3 wt%, the production rates of CO and C₂H₆ reached their highest values of 5.88 and 11.07 $\mu\text{mol g}^{-1} \text{h}^{-1}$, respectively, and the production rates of CO and C₂H₆ were 8.39 times higher than that of pristine CeO₂. The C₂H₆ electron selectivity and production selectivity are 93.1 % and 65.3 %, respectively, for ACEO-3 (Table 1) [27–29]. Moreover, the selectivity of C₂H₆ increased when Au contents increased from 0.5 % to 5 %. The formation of C2 products was determined by the Au-CeO₂ micro-interface, and the increase in the Au content exposed more Au-CeO₂ micro-interface (which was proved via the mechanistic study). When further increasing the Au content to 7 %, more Au nanoparticles would cover the surface of CeO₂, which would make more CO₂ molecules adsorb on Au nanoparticles and transform into CO using hot electrons from Au. Therefore, the selectivity of C₂H₆ turns to be decreased with the 7 % Au content. Notably, compared to recently reported state-of-the-art photocatalysts, ACEO-3 shows better or comparable C2 selectivity and photocatalytic activity (Table S2). As shown in Fig. 2(b), ACEO-3 displayed a slight decrease in photocatalytic stability within 12 h of continuous simulated sunlight irradiation. The evolution rates of C₂H₆ were 11.07, 10.38 and 6.33 $\mu\text{mol g}^{-1} \text{h}^{-1}$, and those of CO were 5.88, 5.92 and 4.76 $\mu\text{mol g}^{-1} \text{h}^{-1}$, respectively, in continual three photocatalytic cycles. However, for CeO₂ (Fig. S12), the CO production in the three cycles is 2.02, 1.81 and 1.77 $\mu\text{mol g}^{-1} \text{h}^{-1}$, respectively, demonstrating a slight decrease in activity. The slight decline in the activities of CeO₂ and ACEO-3 was further analyzed via a series of characterizations (Figs. S13–S15). In the TEM, XRD, and XPS analyses, no significant structural changes were detected. The peak intensities increased at 1451 and 1439 cm^{-1} in the FTIR spectra, which was attributed to the chemisorption of CO₂ and H₂O at the active sites. The results showed that the decrease in stability was due to the occupation of the active sites by CO₂ and H₂O.

Next, the source of C in the carbon products was determined via isotopic ¹³CO₂ labeling experiments with GC–MS under similar test conditions (Fig. 2(c)). Characteristic peaks of $m/z = 29$ and 32 were observed in the ACEO-3 mass spectra, and the intensity ratio was 1:2, which was consistent with the production rate ratio of CO and C₂H₆ (1:1.9). As O₂ was not generated in the oxygen generation experiment (Fig. S16), the characteristic peaks at $m/z = 29$ and 32 were attributed to ¹³CO and ¹³C₂H₆, respectively. This result confirmed that CO₂ was the only C source in this reaction. Control experiments were performed to further study the role of photocatalysts, water, light, and CO₂ (Fig. 2(d)). CO or C₂H₆ was not generated in the absence of photocatalyst, water, light, or CO₂, further demonstrating that these four factors were essential for CO₂ photoreduction. When the catalyst reacted in a N₂

atmosphere, a small amount of CO and C₂H₆ were produced owing to the small amount of CO₂ contained in N₂. Therefore, a gradient experiment using ACEO-3 under low-concentration CO₂ was designed (Fig. 2(e)). The system was first evacuated, followed by the addition of a fixed volume of atmospheric CO₂, and finally filled with N₂ to 80 kPa. Compared with pure CO₂, the carbon production rate was 64.1 % when 5 mL of atmospheric CO₂ was added to N₂. Moreover, with a decrease in CO₂ concentration, the production of carbon products decreased, indicating that ACEO-3 was very sensitive to the CO₂ concentration in N₂. In the air atmosphere, ACEO-3 produced a certain amount of carbon products (CO: 2.09 $\mu\text{mol g}^{-1} \text{h}^{-1}$; C₂H₆: 3.05 $\mu\text{mol g}^{-1} \text{h}^{-1}$), indicating that the catalyst had a high industrial value. To further demonstrate the role of Au and CeO₂ in C₂H₆ generation, Au/CuO, Au/g-C₃N₄, Cu/CeO₂, and Pt/CeO₂ were prepared using the same synthetic method for comparison. As shown in Fig. 2(f), after replacing CeO₂ with CuO or g-C₃N₄, only CO was obtained as the product, confirming that Au could only combine with CeO₂ to generate C2 products. Similarly, after replacing Au with Cu and Pt, only CH₄ and CO were produced, indicating that Au played an important role in forming the C2 product. These results revealed that both Au and CeO₂ were essential for the generation of C2 products.

3.3. Mechanism study of Au-CeO₂ composites

Thereafter, the mechanistic study of the Au-CeO₂ nanocomposite was then performed to disclose its working mechanism for highly efficient generation of C2 products, which include photo-electrochemical behaviors (Fig. 3), in-situ intermediates study (Fig. 4), and theoretical simulations (Figs. 5 and 6).

The UV–vis DRS spectra (Fig. 3(a)) show that ACEO-x exhibit stronger light absorption intensity than pristine CeO₂, which was mainly caused by the LSPR effect of Au. This was also related to the color change of the catalyst (Fig. S3) [5,30]. To verify the role of the LSPR effect of Au in the photoreduction process, light with a wavelength > 420 nm was used for the reaction, and the results are shown in Fig. S17. Carbon products were not observed during the reaction, confirming that the LSPR effect of Au could not act alone. The direct bandgap energies (E_g) of CeO₂ and ACEO-x are calculated as 3.10, 3.10, 3.10, 2.95 and 2.97 eV, respectively, using the Tauc plots (Fig. 3(b)). The conduction band (CB) positions of CeO₂ and ACEO-3 are calculated as −1.59 and −1.20 V versus Normal Hydrogen Electrode (NHE), respectively, and the valence band (VB) positions are 1.51 and 1.75 V versus NHE, respectively, based on the VB-XPS spectra and Mott–Schottky curve (Fig. S18). The resulting schematic of the band structure is shown in Fig. 3(c) [31]. The E⁰ (CO₂/CO = −0.52 V vs. NHE; CO₂/C₂H₆ = −0.27 V vs. NHE) was between the CB and VB [12,32], inferring that CeO₂ and ACEO-3 had a suitable band gap to generate CO and C₂H₆.

To verify the effect of the charge separation efficiency on the catalytic activity, PL spectra were obtained (Fig. S19). ACEO-3 exhibited the highest carrier-separation efficiency. Similarly, in the time-resolved fluorescence spectra (Fig. 3(d) and Table S3), ACEO-3 exhibits the longest carrier lifetime, suggesting that an Au content of 3 % is the most favorable for separating electrons and holes. In addition, ACEO-3 shows a higher photocurrent and smaller arc radius in the photo-electrochemical and EIS analyses (Fig. 3(e)–(f)), which further verified the above results. Although the Au nanocrystals enhance charge separation, they also reduce the CO₂ adsorption capacity (Fig. S20). The Au nanocrystals on the CeO₂ surface hindered the contact between CeO₂ and CO₂, which further improved the performance of ACEO-x and deteriorated the catalytic performance when the Au content was higher than 3 wt%. Combining these observations, compared with pristine CeO₂, the micro-interface in Au-CeO₂ could allow more photo-electrons to participate in the photoreduction reaction and promote the photoreduction activity.

In situ FTIR tests were performed to identify the crucial intermediates of the C2 products (Fig. 4). For ACEO-3, the characteristic

Table 1
Photocatalytic CO₂ reduction performance over various catalysts.

Catalyst	Production rates ($\mu\text{mol g}^{-1} \text{h}^{-1}$)		Electron rates ($\mu\text{mol g}^{-1} \text{h}^{-1}$)		Sel _{product} (%) ^a	Sel _{electron} (%) ^b
	CO	C ₂ H ₆	CO	C ₂ H ₆		
Pristine CeO ₂	2.0	0	4.0	0	0	0
ACEO-0.5	4.5	2.3	9.0	32.2	33.8	78.2
ACEO-1	5.5	5.0	11.0	70.0	21.6	86.4
ACEO-3	5.9	11.1	11.8	159.6	65.3	93.1
ACEO-5	3.7	9.1	7.4	127.4	71.1	94.5

^a Product selectivity (Sel_{product}) of C₂H₆: Sel_{product} (%) = (v(C₂H₆)) / (v(CO) + v(C₂H₆)) × 100 %.

^b Electron selectivity (Sel_{electron}) of C₂H₆: Sel_{electron} (%) = (14 v(C₂H₆)) / (2 v(CO) + 14 v(C₂H₆)) × 100 %; where v(CO) and v(C₂H₆) denote the formation rates of CO, and C₂H₆, respectively.

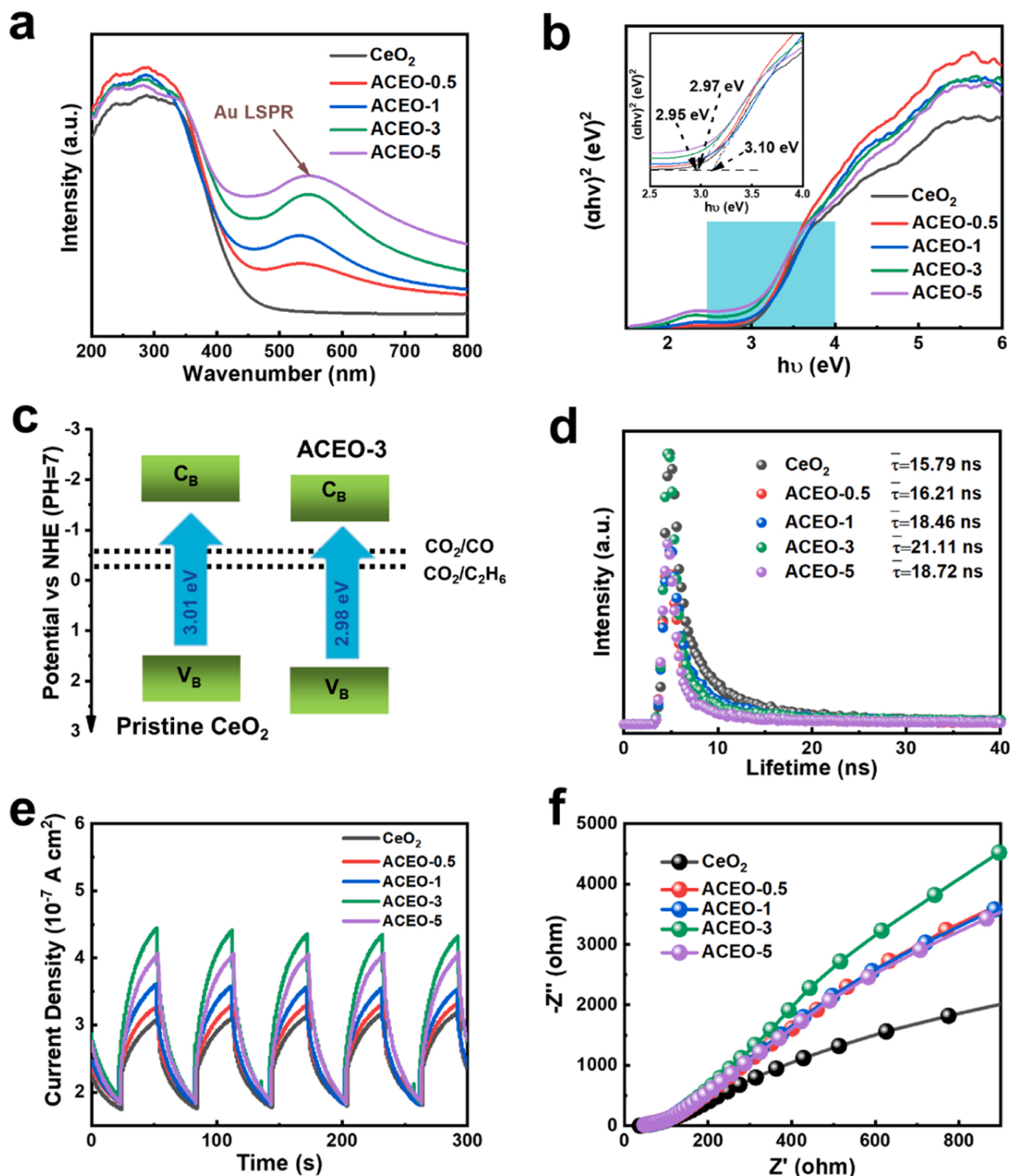


Fig. 3. (a) UV-vis DRS spectra of pristine CeO₂ and ACEO-x. (b) Band gaps of pristine CeO₂ and ACEO-x. (c) Schematic illustrating the electronic band structures; blue arrows represent the electron transition process. CB, conduction band; VB, valence band. (d) Time-resolved fluorescence spectra. (e) Photocurrent response under light irradiation and (f) Electrochemical impedance spectroscopy (EIS) Nyquist plots of the as-obtained samples in the dark.

peaks at 1556 and 1520 cm⁻¹ are attributed to CO₃²⁻*, and H₂O*, respectively (Fig. 4(a)) [13,33]. The intensity of these peaks increased with increasing illumination time, indicating that both CO₂ and H₂O continuously participated in the photoreduction reaction. In addition, important intermediates for the generation of CO were observed, including COOH* (at 1540 and 1620 cm⁻¹) and CO* (at 1713 cm⁻¹) [32,34,35]. Among them, the generation of COOH* was the rate-limiting step of the reaction, and CO* represented the production of CO. Moreover, several important C2 intermediates, such as COCO* (at 1374 and 1486 cm⁻¹) and COCOH* (at 1233 and 1574 cm⁻¹), were observed, providing strong evidence for the generation of C₂H₆ [36–38]. As shown in Fig. 4(b), pristine CeO₂ showed the same characteristic

peaks at 1556 and 1524 cm⁻¹ as ACEO-3, indicating similar reaction paths in the adsorption and initial activation stages of CO₂ molecules. However, for the pristine CeO₂, only the intermediates for CO (COOH* and CO*) were observed, and the C2 intermediates (COCO*, COCOH*) could not be detected, demonstrating that the Au-CeO₂ micro-interface was decisive for the production of C2 intermediates.

Based on the in-situ FTIR spectra in Fig. 4, the CO₂ reduction pathways have been proposed for the ACEO-3 system as follows:



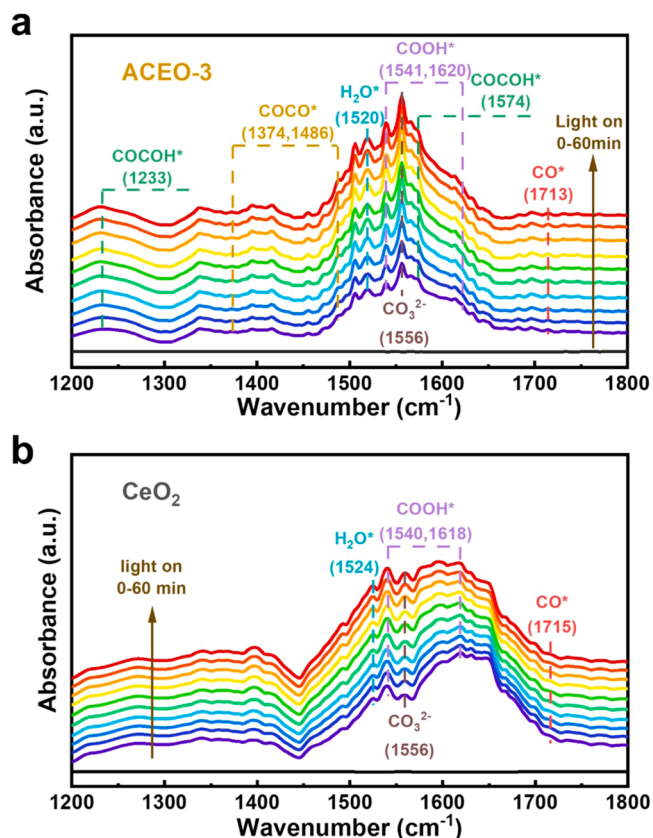


Fig. 4. In situ FTIR spectra for the co-adsorption of a mixture of CO₂ and H₂O vapors over (a) ACEO-3 and (b) CeO₂.



where * and † represent the surface-active sites and the release of gas in the reaction, respectively.

The mechanism of the Au-CeO₂ system was further explored using density functional theory (DFT) calculations. The (111) plane of CeO₂ observed in the TEM image was used for modeling, and Au₃₂ nanoclusters were introduced, in which Au particles and CeO₂ were linked by O atoms. Then, to support the speculation of in situ FTIR, Gibbs free energy calculations were performed to further verify the pathways at the molecular level. First, the active centers of CeO₂ and ACEO-x were determined by comparing the adsorption capacities of metal sites with

O_V for CO₂ (O_V and Au-O-Ce were used in the theoretical models). The results of the Gibbs free energy calculations are presented in Fig. 5(a) and Table S4, where the formation of COOH* and the desorption of CO* were the main rate-limiting steps. The formation of the COOH* intermediate was endothermic and involved a high activation energy barrier. The formation of Au-CeO₂ micro-interface changed the active sites for the reaction, decreasing the COOH* barrier from 1.09 to 0.50 eV. Moreover, the CO* desorption energy of pristine CeO₂ was lower than that of ACEO-x, but ACEO-x exhibited a high CO yield because Au-O-Ce could promote the production of COOH*. In addition, based on the results presented in Table S5, after the adsorption of CO₂ by CeO₂ and ACEO-x, the bond angle of the CO₂ molecule decreased, and the bond length increased, facilitating the breakage of the C=O bond.

To further study the mechanism of C-C coupling, the energy barriers for CO* to generate COCO* were calculated, which were 1.02 and 0.64 eV for pristine CeO₂ and ACEO-3, respectively. It was easier to generate COCO* from CO* at ACEO-x instead of desorbing CO* to carbon monoxide, revealing that the Au-O-Ce played a decisive role in C-C coupling. The Gibbs free energies and structures of C2 intermediates for ethane production are shown in Figs. S21–S23. The significant reduction in the formation energies of COOH* and COCO* intermediates during CO₂ reduction is the key step in the photocatalytic production of C₂H₆; the former promoted the generation of massive amounts of CO* intermediates, and the latter stabilized the COCO* intermediates. Both acted synergically to ensure that CO* multi-electron reduction was performed before desorption. Therefore, the change in Gibbs free energy confirmed the crucial role of Au-O-Ce at the Au-CeO₂ micro-interface in the photocatalytic reduction of CO₂ to C₂ species.

In addition, based on the DFT calculations, the top VB of the total density of states (TDOS) in pristine CeO₂ is mainly attributed to the orbital of O in Fig. 5(b), and the bottom CB mainly corresponds to the orbital of Ce. Considering the partial density of states (PDOS), the O 2p and Ce 4f orbitals play a major role in VB and CB (Fig. 5(c)), respectively. The top VB from the TDOS in ACEO-x is mainly composed of the orbitals of Au and O elements in Fig. 5(d), indicating a connection between Au and O atoms. The bottom CB of ACEO-x was the same as that of pristine CeO₂. To further study the orbital hybridization of Au and O atoms, the PDOS was calculated, as shown in Fig. 5(e). The O 2p orbital almost coincided with the Au 5d orbital, suggesting a p-d orbital hybrid [31]. The strong electronic interaction between Au and O immobilized the Au nanocrystals on CeO₂, which further supported the XPS results.

Additionally, the Bader charge and differential charge distributions indicate that before CO₂ adsorption, the surrounding Au atoms are the main charge enrichment sites (Fig. S24). After CO₂ adsorption (Fig. 6(a)), electrons flow from Au atoms to adjacent CO₂, so that all CO₂ molecules were in a region of high charge concentration (Table S6), which is the premise of C-C coupling. Compared to ACEO-x, the electrons of pristine CeO₂ are more concentrated at the oxygen atoms of CO₂ (Fig. 6(b)). Combining the above observations, C₂ products could be generated only in the presence of the Au-CeO₂ micro-interface because Au-O-Ce could induce a large number of electrons around C atoms. Based on the TDOS comparison of pristine CeO₂ and ACEO-x, adding Au reduced the band gap, which was consistent with the results in Fig. 3(c).

4. Conclusion

In summary, the Au-O-Ce active sites in the nanocomposite of noble metals Au and CeO₂ exhibit high activity at the micro-interface and are favorable for the selective photoreduction of CO₂ to C₂H₆. First, the formation of a micro-interface was confirmed via HADDF-STEM and XPS. The mechanism of photoreduction was explained using in-situ FTIR analysis and DFT theoretical calculations. The Au-CeO₂ micro-interface promoted C-C coupling by gathering a large number of electrons around the C atoms and reducing the energy barriers to generate COOH* and COCO*. Consequently, the photoreduction of CO₂ to C₂H₆ was selectively prompted by the Au-CeO₂ nanocomposite. A high electron

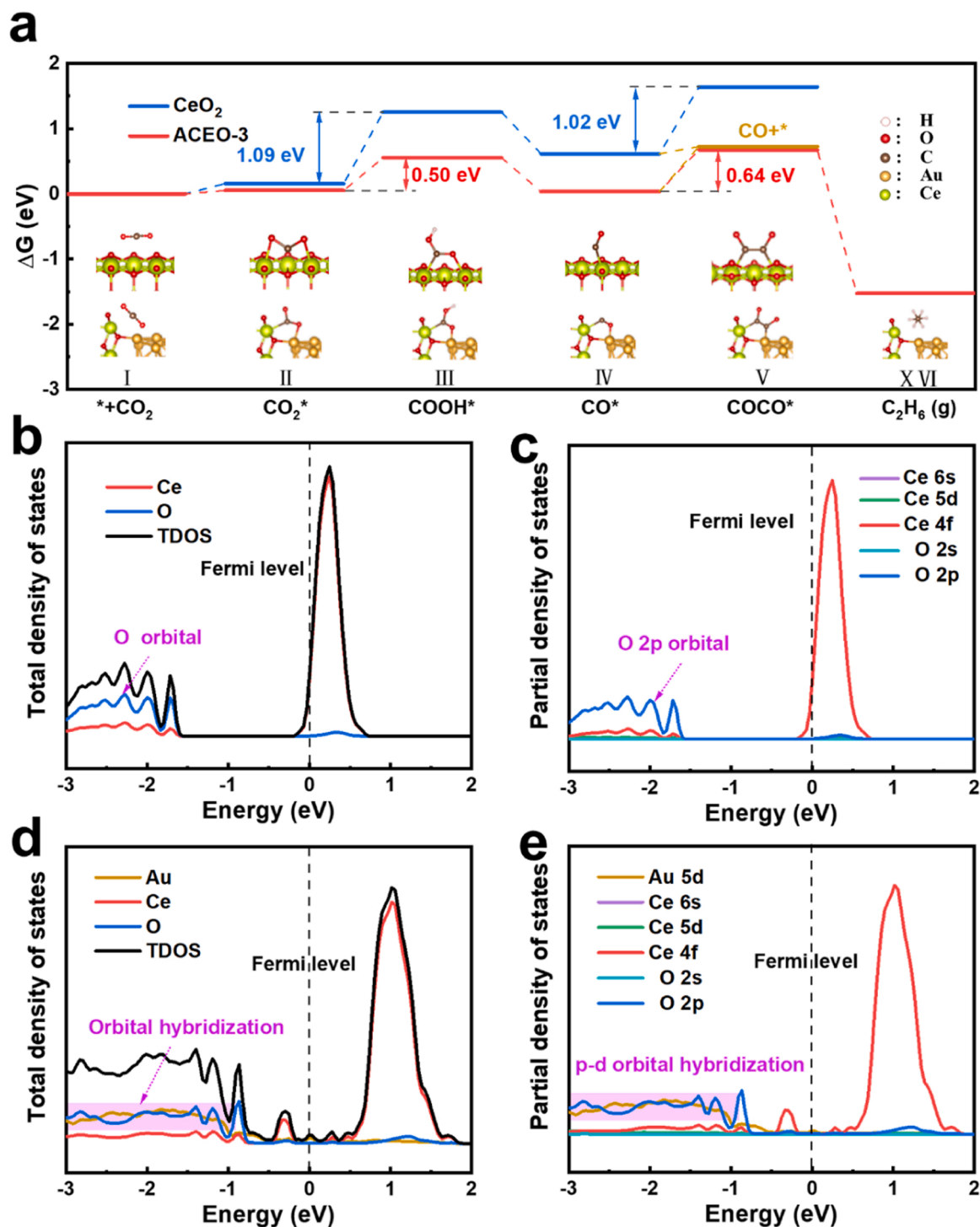


Fig. 5. (a) Reaction pathways for Gibbs free energy calculations for photocatalytic CO₂ reduction. (b) Total density of states and total orbital distribution of each element on CeO₂ and the corresponding (c) projected density of states for O 2s, O 2p, Ce 6s, Ce 5d, and Ce 4f orbital distribution. (d) Total density of states and total orbital distribution of each element on ACEO-x and the corresponding (e) projected density of states for O 2s, O 2p, Ce 6s, Ce 5d, Ce 4f, and Au 5d orbital distribution.

selectivity of 93.1 % was achieved for C₂H₆ (product selectivity of 65.3 %), and the yield of C₂H₆ increased from 0 to 11.8 $\mu\text{mol g}^{-1} \text{h}^{-1}$. This study confirms that the micro-interface generated by noble metals and rare-earth oxides can promote the formation of C₂ products by changing the active sites. It provides a new strategy to design future catalysts for CO₂ photoreduction to C₂ products.

CRediT authorship contribution statement

Jixiang Ji: Formal analysis, Writing – original draft. **Ruru Li:** Investigation, Formal analysis. **Hao Zhang:** Investigation, Formal analysis. **Yingnan Duan:** Investigation, Formal analysis. **Qian Liu:** Investigation, Formal analysis. **Haozhi Wang:** Conceptualization, Supervision. **Zhurui Shen:** Conceptualization, Methodology, Supervision.

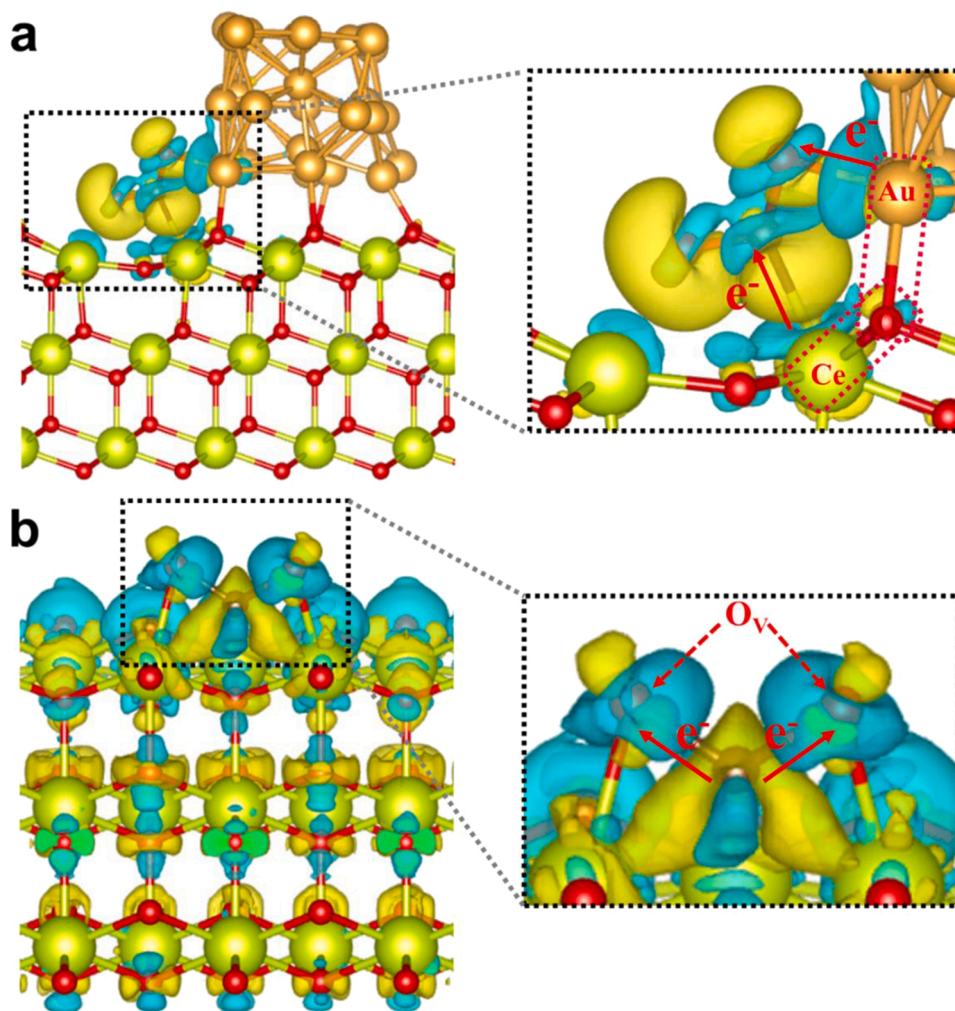


Fig. 6. Differential charge density calculations for (a) CeO_2 and (b) ACEO-x. Blue regions represent charge accumulation; yellow regions represent charge loss; C, Ce, O, and Au atoms are represented as brown, yellow, red, and gold spheres, respectively.

Declaration of Competing Interest

The authors declare that they have no known competing financial interests or personal relationships that could have appeared to influence the work reported in this paper.

Data Availability

Data will be made available on request.

Acknowledgements

This work was supported by the grants from the Fundamental Research Funds for the Central Universities, Nankai University (ZB19100141), the National Natural Science Foundation of China (21872102 and 22172080) and the Tianjin “Project + Team” innovation team, 2020.

Appendix A. Supporting information

Supplementary data associated with this article can be found in the online version at [doi:10.1016/j.apcatb.2022.122020](https://doi.org/10.1016/j.apcatb.2022.122020).

References

- [1] Z. Jiang, X. Xu, Y. Ma, H.S. Cho, D. Ding, C. Wang, J. Wu, P. Oleynikov, M. Jia, J. Cheng, Y. Zhou, O. Terasaki, T. Peng, L. Zan, H. Deng, Filling metal-organic framework mesopores with TiO_2 for CO_2 photoreduction, *Nature* 586 (2020) 549–554.
- [2] Y. Li, D. Hui, Y. Sun, Y. Wang, Z. Wu, C. Wang, J. Zhao, Boosting thermo-photocatalytic CO_2 conversion activity by using photosynthesis-inspired electron-proton-transfer mediators, *Nat. Commun.* 12 (2021) 123.
- [3] Y. Shi, J. Li, C. Mao, S. Liu, X. Wang, X. Liu, S. Zhao, X. Liu, Y. Huang, L. Zhang, Van Der Waals gap-rich BiOCl atomic layers realizing efficient, pure-water CO_2 -to- CO photocatalysis, *Nat. Commun.* 12 (2021) 5923.
- [4] N. Li, X. Chen, J. Wang, X. Liang, L. Ma, X. Jing, D.-L. Chen, Z. Li, ZnSe nanorods- CsSnCl_3 perovskite heterojunction composite for photocatalytic CO_2 reduction, *ACS Nano* 16 (2022) 3332–3340.
- [5] X. Jiang, J. Huang, Z. Bi, W. Ni, G. Gurzadyan, Y. Zhu, Z. Zhang, Plasmonic active “hot spots”-confined photocatalytic CO_2 reduction with high selectivity for CH_4 production, *Adv. Mater.* 34 (2022), 2109330.
- [6] T. Yan, N. Li, L. Wang, W. Ran, P.N. Duchesne, L. Wan, N.T. Nguyen, L. Wang, M. Xia, G.A. Ozin, Bismuth atom tailoring of indium oxide surface frustrated Lewis pairs boosts heterogeneous CO_2 photocatalytic hydrogenation, *Nat. Commun.* 11 (2020) 6095.
- [7] A. Hezam, K. Namratha, Q.A. Drmash, D. Ponnamm, J. Wang, S. Prasad, M. Ahmed, C. Cheng, K. Byrappa, CeO_2 nanostructures enriched with oxygen vacancies for photocatalytic CO_2 reduction, *ACS Appl. Nano Mater.* 3 (2020) 138–148.
- [8] Y. Xia, K. Xiao, B. Cheng, J. Yu, L. Jiang, M. Antonietti, S. Cao, Improving artificial photosynthesis over carbon nitride by gas-liquid-solid interface management for full light-induced CO_2 reduction to C1 and C2 fuels and O_2 , *ChemSusChem* 13 (2020) 1730–1734.
- [9] Q. Chen, X. Chen, M. Fang, J. Chen, Y. Li, Z. Xie, Q. Kuang, L. Zheng, Photo-induced Au-Pd alloying at TiO_2 {101} facets enables robust CO_2 photocatalytic reduction into hydrocarbon fuels, *J. Mater. Chem. A* 7 (2019) 1334–1340.

- [10] F. Yu, X. Jing, Y. Wang, M. Sun, C. Duan, Hierarchically porous metal–organic framework/MoS₂ interface for selective photocatalytic conversion of CO₂ with H₂O into CH₃COOH, *Angew. Chem., Int. Ed.* 60 (2021) 24849–24853.
- [11] S. Zhu, X. Li, X. Jiao, W. Shao, L. Li, X. Zu, J. Hu, J. Zhu, W. Yan, C. Wang, Y. Sun, Y. Xie, Selective CO₂ photoreduction into C₂ product enabled by charge-polarized metal pair sites, *Nano Lett.* 21 (2021) 2324–2331.
- [12] K. Wang, J. Lu, Y. Lu, C.H. Lau, Y. Zheng, X. Fan, Unravelling the C–C coupling in CO₂ photocatalytic reduction with H₂O on Au/TiO₂-x: Combination of plasmonic excitation and oxygen vacancy, *Appl. Catal. B Environ.* 292 (2021) 120147.
- [13] W. Wang, C. Deng, S. Xie, Y. Li, W. Zhang, H. Sheng, C. Chen, J. Zhao, Photocatalytic C–C coupling from carbon dioxide reduction on copper oxide with mixed-valence copper(I)/copper(II), *J. Am. Chem. Soc.* 143 (2021) 2984–2993.
- [14] E. Vahidzadeh, S. Zeng, A.P. Manuel, S. Riddell, P. Kumar, K.M. Alam, K. Shankar, Asymmetric multipole plasmon-mediated catalysis shifts the product selectivity of CO₂ photoreduction toward C₂+ products, *ACS Appl. Mater. Interfaces* 13 (2021) 7248–7258.
- [15] Y. Yu, X. Dong, P. Chen, Q. Geng, H. Wang, J. Li, Y. Zhou, F. Dong, Synergistic effect of Cu single atoms and Au–Cu alloy nanoparticles on TiO₂ for efficient CO₂ photoreduction, *ACS Nano* 15 (2021) 14453–14464.
- [16] N. Rui, X. Zhang, F. Zhang, Z. Liu, X. Cao, Z. Xie, R. Zou, S.D. Senanayake, Y. Yang, J.A. Rodriguez, C.-J. Liu, Highly active Ni/CeO₂ catalyst for CO₂ methanation: preparation and characterization, *Appl. Catal. B Environ.* 282 (2021), 119581.
- [17] R. Ryoo, J. Kim, C. Jo, S.W. Han, J.-C. Kim, H. Park, J. Han, H.S. Shin, J.W. Shin, Rare-earth–platinum alloy nanoparticles in mesoporous zeolite for catalysis, *Nature* 585 (2020) 221–224.
- [18] D.F. Sava Gallis, D.J. Vogel, G.A. Vincent, J.M. Rimsza, T.M. Nenoff, NO_x adsorption and optical detection in rare earth metal–organic frameworks, *ACS Appl. Mater. Interfaces* 11 (2019) 43270–43277.
- [19] S. Zhang, Z.C. Zeng, Q.Q. Li, B.L. Huang, X.Y. Zhang, Y.P. Du, C.H. Yan, Lanthanide electronic perturbation in Pt–Ln (La, Ce, Pr and Nd) alloys for enhanced methanol oxidation reaction activity, *Energy Environ. Sci.* 14 (2021) 5911–5918.
- [20] Z. Liang, L.L. Yin, H. Yin, Z.Y. Yin, Y.P. Du, Rare earth element based single-atom catalysts: synthesis, characterization and applications in photo/electro-catalytic reactions, *Nanoscale Horiz.* 7 (2022) 31–40.
- [21] X. Huang, K. Zhang, B. Peng, G. Wang, M. Muhler, F. Wang, Ceria-based materials for thermocatalytic and photocatalytic organic synthesis, *ACS Catal.* 11 (2021) 9618–9678.
- [22] M. Wang, M. Shen, X. Jin, J. Tian, M. Li, Y. Zhou, L. Zhang, Y. Li, J. Shi, Oxygen vacancy generation and stabilization in CeO_{2-x} by Cu introduction with improved CO₂ photocatalytic reduction activity, *ACS Catal.* 9 (2019) 4573–4581.
- [23] Z. Wang, J. Zhu, X. Zu, Y. Wu, S. Shang, P. Ling, P. Qiao, C. Liu, J. Hu, Y. Pan, J. Zhu, Y. Sun, Y. Xie, Selective CO₂ photoreduction to CH₄ via Pd^{δ+}-assisted hydrodeoxygenation over CeO₂ nanosheets, *Angew. Chem., Int. Ed.* 61 (2022), e202203249.
- [24] L. Lei, H. Liu, Z. Wu, Z. Qin, G. Wang, J. Ma, L. Luo, W. Fan, J. Wang, Aerobic oxidation of alcohols over isolated single Au atoms supported on CeO₂ nanorods: catalysis of interfacial [O–Ov–Ce–O–Au] sites, *ACS Appl. Nano Mater.* 2 (2019) 5214–5223.
- [25] P.F. Wang, Y.S. Mao, L.N. Li, Z.R. Shen, X. Luo, K.F. Wu, P.F. An, H.T. Wang, L. N. Su, Y. Li, S.H. Zhan, Unraveling the interfacial charge migration pathway at the atomic level in a highly efficient Z-scheme photocatalyst, *Angew. Chem. Int. Ed.* 58 (2019) 11329–11334.
- [26] J. Kong, Z. Xiang, G. Li, T. An, Introduce oxygen vacancies into CeO₂ catalyst for enhanced coke resistance during photothermocatalytic oxidation of typical VOCs, *Appl. Catal. B Environ.* 269 (2020), 118755.
- [27] J. Li, H. Huang, W. Xue, K. Sun, X. Song, C. Wu, L. Nie, Y. Li, C. Liu, Y. Pan, H.-L. Jiang, D. Mei, C. Zhong, Self-adaptive dual-metal-site pairs in metal-organic frameworks for selective CO₂ photoreduction to CH₄, *Nat. Catal.* 4 (2021) 719–729.
- [28] H. Huang, R. Shi, Z. Li, J. Zhao, C. Su, T. Zhang, Triphase photocatalytic CO₂ reduction over silver-decorated titanium oxide at a gas–water boundary, *Angew. Chem., Int. Ed.* 61 (2022), e202200802.
- [29] Y. Jiang, H.-Y. Chen, J.-Y. Li, J.-F. Liao, H.-H. Zhang, X.-D. Wang, D.-B. Kuang, Z-Scheme 2D/2D Heterojunction of CsPbBr₃/Bi₂WO₆ for Improved Photocatalytic CO₂ Reduction, *Adv. Funct. Mater.* 30 (2020), 2004293.
- [30] B. Gerislioglu, L. Dong, A. Ahmadiwand, H. Hu, P. Nordlander, N.J. Halas, Monolithic metal dimer-on-film structure: new plasmonic properties introduced by the underlying metal, *Nano Lett.* 20 (2020) 2087–2093.
- [31] P. Chen, B. Lei, X. Dong, H. Wang, J. Sheng, W. Cui, J. Li, Y. Sun, Z. Wang, F. Dong, Rare-earth single-atom La–N charge-transfer bridge on carbon nitride for highly efficient and selective photocatalytic CO₂ reduction, *ACS Nano* 14 (2020) 15841–15852.
- [32] X. Li, Y. Sun, J. Xu, Y. Shao, J. Wu, X. Xu, Y. Pan, H. Ju, J. Zhu, Y. Xie, Selective visible-light-driven photocatalytic CO₂ reduction to CH₄ mediated by atomically thin CuIn₅S₈ layers, *Nat. Energy* 4 (2019) 690–699.
- [33] L. Cheng, X. Yue, L. Wang, D. Zhang, P. Zhang, J. Fan, Q. Xiang, Dual-single-atom tailoring with bifunctional integration for high-performance CO₂ photoreduction, *Adv. Mater.* 33 (2021), 2105135.
- [34] Y. Shi, G. Zhan, H. Li, X. Wang, X. Liu, L. Shi, K. Wei, C. Ling, Z. Li, H. Wang, C. Mao, X. Liu, L. Zhang, Simultaneous manipulation of bulk excitons and surface defects for ultrastable and highly selective CO₂ photoreduction, *Adv. Mater.* 33 (2021), 2100143.
- [35] X.-F. Qiu, H.-L. Zhu, J.-R. Huang, P.-Q. Liao, X.-M. Chen, Highly selective CO₂ electroreduction to C₂H₄ using a metal–organic framework with dual active sites, *J. Am. Chem. Soc.* 143 (2021) 7242–7246.
- [36] J. Zhu, W. Shao, X. Li, X. Jiao, J. Zhu, Y. Sun, Y. Xie, Asymmetric triple-atom sites confined in ternary oxide enabling selective CO₂ photothermal reduction to acetate, *J. Am. Chem. Soc.* 143 (2021) 18233–18241.
- [37] T. Cheng, A. Fortunelli, W.A. Goddard III, Reaction intermediates during operando electrocatalysis identified from full solvent quantum mechanics molecular dynamics, *Proc. Natl. Acad. Sci. USA* 116 (2019) 7718–7722.
- [38] E. Pérez-Gallent, M.C. Figueiredo, F. Calle-Vallejo, M.T.M. Koper, Spectroscopic observation of a hydrogenated CO dimer intermediate during CO reduction on Cu (100) electrodes, *Angew. Chem. Int. Ed.* 56 (2017) 3621–3624.